

# Experiment to Form and Characterize a Section of a Spherically Imploding Plasma Liner

S. C. Hsu<sup>1</sup>, S. J. Langendorf, K. C. Yates, J. P. Dunn, S. Brockington, A. Case, E. Cruz, F. D. Witherspoon, M. A. Gilmore, J. T. Cassibry<sup>2</sup>, R. Samulyak, P. Stoltz, K. Schillo, W. Shih, K. Beckwith, and Y. C. F. Thio

**Abstract**—We describe an experiment to form and characterize a section of a spherically imploding plasma liner by merging six supersonic plasma jets that are launched by newly designed contoured-gap coaxial plasma guns. This experiment is a prelude to forming a fully spherical imploding plasma liner using many dozens of plasma guns, as a standoff driver for plasma-jet-driven magnetoinertial fusion. The objectives of the six-jet experiments are to assess the evolution and scalings of liner Mach number and uniformity, which are important metrics for spherically imploding plasma liners to compress magnetized target plasmas to fusion conditions. This paper describes the design of the coaxial plasma guns, experimental characterization of the plasma jets, six-jet experimental setup and diagnostics, initial diagnostic data from three- and six-jet experiments, and the high-level objectives of associated numerical modeling.

**Index Terms**—Plasma applications, plasmas.

## I. INTRODUCTION

**S**PHERICALLY imploding plasma liners formed by merging supersonic plasma jets are a proposed low-cost, high-shot-rate, standoff driver for plasma-jet-driven magnetoinertial fusion (PJMIF) [1]–[3]. MIF [4]–[6] seeks to achieve fusion at ion densities intermediate between those of magnetic and inertial fusion, by combining attributes of both the latter approaches. The primary near-term objective of the plasma liner experiment (PLX) [2], [7] is to demonstrate the formation of spherically imploding plasma liners by merging dozens of supersonic plasma jets and to demonstrate their viability and scalability toward reactor-relevant energies and scales.

Manuscript received September 29, 2017; accepted November 29, 2017. Date of publication December 18, 2017; date of current version June 8, 2018. This work was supported by the Advanced Research Projects Agency–Energy, U.S. Department of Energy. The review of this paper was arranged by Senior Editor S. J. Gitomer. (Corresponding author: S. C. Hsu.)

S. C. Hsu, S. J. Langendorf, and J. P. Dunn are with the Physics Division, Los Alamos National Laboratory, Los Alamos, NM 87545 USA (e-mail: scotthsu@lanl.gov).

K. C. Yates and M. A. Gilmore are with the Electrical and Computer Engineering Department, University of New Mexico, Albuquerque, NM 87131 USA.

S. Brockington, A. Case, E. Cruz, and F. D. Witherspoon are with HyperV Technologies Corp., Chantilly, VA 20151 USA, and also with HyperJet Fusion Corporation, Chantilly, VA 20151 USA.

J. T. Cassibry and K. Schillo are with the Propulsion Research Center, University of Alabama in Huntsville, Huntsville, AL 35899 USA.

R. Samulyak and W. Shih are with the Department of Applied Mathematics and Statistics, Stony Brook University, Stony Brook, NY 11794 USA.

P. Stoltz is with Tech-X Corporation, Boulder, CO 80303 USA.

K. Beckwith was with Tech-X Corporation, Boulder, CO 80303 USA. He is now with Sandia National Laboratories, Albuquerque, NM 87185 USA.

Y. C. F. Thio is with HyperJet Fusion Corporation, Chantilly, VA 20151 USA.

Color versions of one or more of the figures in this paper are available online at <http://ieeexplore.ieee.org>.

Digital Object Identifier 10.1109/TPS.2017.2779421

The PLX facility was built in 2010–2011 at the Los Alamos National Laboratory (LANL) to study plasma-liner formation via merging supersonic plasma jets [2], [8]. From 2011 to 2014, the PLX utilized parallel-plate mini-railguns [9]–[12], designed and built by HyperV Technologies Corp. in a series of experiments [7] to study single-jet propagation [13], two-jet oblique merging [14], [15], and two-jet head-on merging [16]. These experiments, with the aid of associated numerical modeling [14], [17], led to the following key results of relevance to the physics of plasma-liner formation: 1) confirmation of plasma-jet parameters and characterization of their evolution and profiles, during approximately 1 m of jet propagation away from the rail-gun nozzle [13]; 2) identification and characterization of collisional-plasma-shock formation between two obliquely merging plasma jets [14], [15], largely consistent with the hydrodynamic oblique shock theory; and 3) the role of rising mean-charge-state  $\bar{Z}$  in keeping the dynamics between merging jets in a collisional regime (because of the  $\bar{Z}^{-4}$  dependence of the counterstreaming ion–ion mean free path) [16]. In parallel, additional theory and modeling efforts examined plasma-liner radial convergence and scalings in 1-D [18]–[22], and the effects of discrete jet merging on plasma-liner convergence in 3-D [23]–[25].

Collectively, these prior studies set the stage for the present PLX- $\alpha$  project, which is named after the Accelerating Low-Cost Plasma Heating and Assembly (ALPHA) Program of the Advanced Research Projects Agency–Energy (ARPA-E) that sponsors this research. The primary objective of PLX- $\alpha$  by the end of the ALPHA Program is to form and study a fully spherical imploding plasma liner with at least 36 and up to 60 merging plasma jets (Fig. 1) that are launched by newly designed coaxial plasma guns fabricated by HyperV Technologies Corp., which is now owned by new fusion startup HyperJet Fusion Corporation. Development of novel,  $\beta > 1$  (where  $\beta$  is the ratio of thermal-to-magnetic pressure) magnetized plasma targets [26] for PJMIF is at a nascent stage and discussed elsewhere [2], [27], [28]. In future experiments involving plasma-liner compression of magnetized plasma targets, we envision using a subset of the same coaxial guns (that form the liner) to form an inertially confined dense plasma target ( $\sim 10^{18} \text{ cm}^{-3}$ ) and to potentially magnetize the target ( $\beta > 1$ ,  $\omega\tau \gtrsim 1$ , where  $\omega\tau$  is the Hall magnetization parameter) using laser beat-wave current drive [27], [28].

The remainder of this paper is organized as follows. Section II describes the design of the new PLX- $\alpha$  coaxial plasma guns and experimental data characterizing the plasma

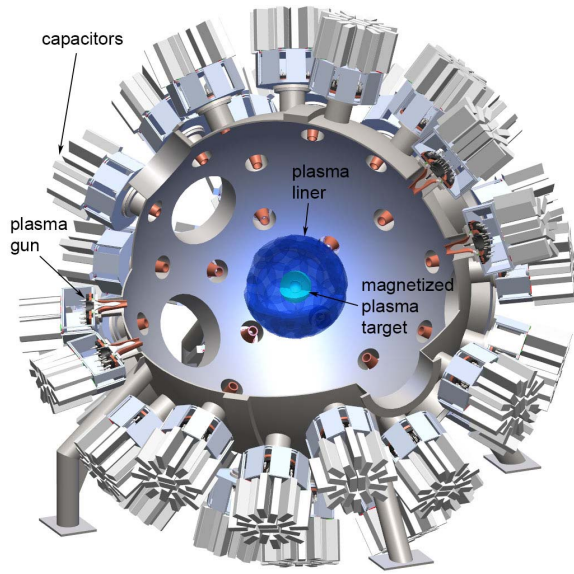


Fig. 1. Illustration of the PLX- $\alpha$  experimental setup, which will ultimately have at least 36 and up to 60 (as shown) coaxial plasma guns mounted around a 2.74-m-diameter vacuum chamber. Shown are plasma guns with integrated capacitor banks and a spherically imploding plasma liner compressing a magnetized plasma target. The PLX- $\alpha$  project is focused on developing the plasma liner and is not addressing the plasma target.

jets that they launch. Section III describes the motivation, experimental/diagnostic setups, and initial diagnostic results of three- and six-gun experiments (a predecessor to the spherical plasma-liner-formation experiments using 36–60 guns). Section IV provides a brief overview of the PLX- $\alpha$  numerical-modeling objectives. Finally, Section V provides a summary and description of future plans.

## II. PLX- $\alpha$ COAXIAL PLASMA GUNS

New contoured-gap coaxial plasma guns were designed and fabricated for the PLX- $\alpha$  project. The rationale for the contoured-gap coaxial-gun concept with preionized mass injection for launching high-mass, high-density jets to  $>50$  km/s was previously laid out in a series of seminal works [29]–[31]. The design of the new PLX- $\alpha$  coaxial guns was governed by the need to achieve particular plasma-jet performance parameters to meet requirements of the PLX- $\alpha$  project (see Section II-A), while establishing a basis for a gun design that could be further developed and scaled up to become fusion-relevant.

### A. Plasma-Jet Requirements

Plasma-jet requirements were determined largely based on the desire to build the lowest cost experiment that would allow studies of plasma-liner formation and convergence in reactor-relevant physics limits inferred from the parameter regimes studied in [3]. These limits are: 1) plasma-jet merging occurs in the collisional limit, i.e., the jet interpenetration depth is small compared with the jet radius; 2) the plasma equation-of-state (EOS) has sufficient ionization and excitation states to provide a significant energy sink (including strong radiative losses) compared with the thermal energy of the jet; and

TABLE I  
REQUIRED AND ACHIEVED ARGON PLASMA-JET PARAMETERS OF THE NEW PLX- $\alpha$  COAXIAL PLASMA GUNS. DETAILS REGARDING THE MEASUREMENT OF JET PARAMETERS ARE GIVEN IN SECTION II-C

Parameter	Required	Achieved
Density	$\approx 2 \times 10^{16} \text{ cm}^{-3}$	$> 2 \times 10^{16} \text{ cm}^{-3}$
Mass	$> 1 \text{ mg}$	$0.47 \pm 0.11 \text{ mg}$
Velocity	$\geq 50 \text{ km/s}$	$52.5 \pm 5.1 \text{ km/s}$
Length	$\leq 10 \text{ cm}$	$16 \pm 5.7 \text{ cm}$

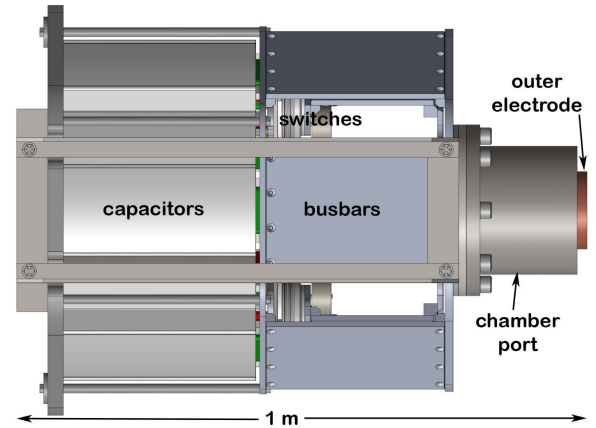


Fig. 2. Illustration of the PLX- $\alpha$  coaxial gun with integrated pulsed-power components (see also Fig. 7).

3) the plasma flow is strongly supersonic, i.e., the sonic Mach number  $M \equiv V_{\text{jet}}/C_s \gtrsim 10$ , where  $V_{\text{jet}}$  is the directed jet speed and  $C_s$  the jet internal sound speed. Requirements 1) and 3) lead to minimum allowable jet density and velocity, respectively. Requirements 2) and 3) necessitate the use of heavier species, such as Ar, Kr, or Xe, though we use lighter elements as well for establishing a scaling database. Table I summarizes the required and achieved plasma-jet parameters of the PLX- $\alpha$  guns. Further discussion of the achieved plasma-jet parameters is presented in Section II-C.

### B. Coaxial-Gun Design

To fulfill these requirements, we exploited prior HyperV gun-development efforts that had already led to: 1) linear railguns capable of achieving the plasma-jet parameters with regard to mass, density, and velocity [7], [10] and 2) coaxial guns with much lower current density that used ablative mass injection [31]. The new PLX- $\alpha$  guns essentially combine the plasma-jet performance and gaseous injection of the railguns with the coaxial electrode geometry of the coaxial guns.

Fig. 2 shows a full-assembly drawing of the new PLX- $\alpha$  coaxial gun and its integrated pulsed-power module. We chose to mount the capacitors that drive the main gun-electrode discharge onto the back of each gun both to minimize inductance and to eliminate the complexity and cost of requiring many parallel transmission lines. Details of the electrodes [Fig. 2 (right)] (hidden from view) are proprietary information of HyperJet Fusion Corporation. The contours on both the outer and inner electrode surfaces were designed based on a series of MACH2 [32] simulations that led to the desired,

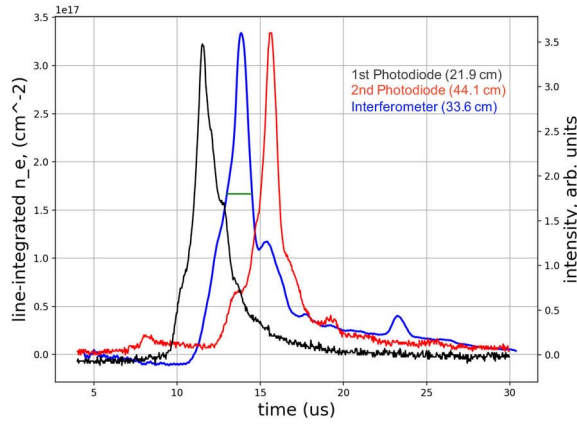


Fig. 3. Interferometer ( $\text{cm}^{-2}$ ) and photodiode (arb.) signals versus time (HyperV shot 201704251255) for transverse views across the plasma jet at various distances (as indicated in the legend) from the exit of the gun. The HyperV interferometer is a quadrature, heterodyne system using a 623-nm He-Ne laser modulated at 110 MHz [33], and the photodiode array is similar to the system described in Section III-A.

calculated plasma-jet parameters. The primary function of the contours is to eliminate the “blowby instability” [30], which must be avoided in order to accelerate high-mass jets.

The guns each have a fast gas valve (GV) mounted at the rear end of the inner electrode to minimize gas travel distance from the GV to the breech (i.e., the coaxial gap at the rear end of the gun) and also 20 tungsten “ignitor pins” [i.e., preionizers (PIs)] distributed uniformly in the azimuthal direction around the breech. The GVs are typically pressurized at up to 20 psig (for the three- and six-gun experiments described in Section III) using any gas or mixture available in a compressed-gas bottle (Ar has been our primary working gas, but we also use  $\text{H}_2$ , He,  $\text{N}_2$ , Ne, Kr, and Xe on PLX). Details of the GV and PI designs are proprietary information of HyperJet Fusion Corporation.

The gun firing sequence is as follows. All the capacitor banks are first charged to the desired voltages (see Sections II-C and III-A for typical values). The GV is triggered first at  $t \approx -600 \mu\text{s}$  (for Ar) to fill the gun breech with neutral gas. Then the PI system is fired at  $t \approx -20 \mu\text{s}$  to ionize the gas fill, and finally the main gun bank is triggered (defined to be  $t = 0$ ) to accelerate the ionized plasma out of the coaxial gun. Gun performance can be tuned by varying the GV fill pressure, capacitor-bank voltages, and GV and PI trigger times.

### C. Plasma-Jet Characterization

Experimental studies of single-plasma-jet performance were performed at HyperV Technologies in order to optimize jet performance and to make progress toward meeting the requirements given in Table I. Jet reproducibility was assessed and the bank voltage and trigger times optimized over a 368-shot campaign firing a single coaxial gun using argon. During this campaign, the gun fired correctly at the triggered time with better than 97.5% reliability.

Fig. 3 shows representative photodiode and interferometry data from transverse views at various distances downstream from the exit of the gun. These measurements were used to

infer jet velocity, length, peak density, and mass as follows. The time delay between the photodiode signals gives the jet velocity (53 km/s). The full-width, half-maximum (FWHM) of the interferometer signal, along with the velocity, gives the jet length (7.8 cm). Assuming a jet diameter of 15 cm at the viewing position (33.6 cm downstream of the exit of the gun), the peak electron density  $n_e$  at that position ( $2.2 \times 10^{16} \text{ cm}^{-3}$ ) is estimated by dividing the peak line-integrated electron density  $\langle n_e \ell \rangle \approx 3.3 \times 10^{17} \text{ cm}^{-2}$  by the diameter, and integration of the interferometer signal over the FWHM gives the FWHM jet mass (0.8 mg). The peak  $n_e$  at the gun exit would be much higher (prior to any spreading of the jet). Table I shows the averaged parameters and standard deviations achieved over 15 shots with the following settings:  $V_{\text{gun}} = -4.7 \text{ kV}$  (center gun electrode charged negatively),  $V_{\text{GV}} = 8.4 \text{ kV}$ ,  $V_{\text{PI}} = 28 \text{ kV}$ ,  $t_{\text{GV}} = -600 \mu\text{s}$ , and 10-psig-Ar GV pressure.

As seen in Table I, the averaged jet performance is close to the requirements but a little shy for jet mass and length. An upgraded GV (rev. 10), now being tested at HyperV, allows much higher gas-fill pressure ( $>50 \text{ psig}$ ), which is expected to help satisfy both the jet mass and length requirements in future experiments. The new GV is also intended to improve jet-to-jet balance as discussed in Section III-B4.

### III. PLX- $\alpha$ THREE- AND SIX-GUN EXPERIMENTS

The first phase of the PLX- $\alpha$  project, in addition to coaxial-gun development and testing at HyperV Technologies, also includes six-gun experiments at LANL (Fig. 4) in order to: 1) successfully operate six guns simultaneously as a demonstration of technical readiness to perform experiments using 36–60 guns for spherical plasma-liner formation and 2) assess the effects of discrete jet merging on plasma-liner formation that could cause significant degradations from 1-D imploding-plasma-liner performance [3], [34]. These jet-merging effects include  $M$ -degradation due to shock heating and seeding of nonuniformities that could exacerbate deceleration-phase instabilities at the liner/target interface (in future, integrated liner-on-target experiments). The instabilities could lead to liner/target mix and reduce the overall effectiveness of plasma liners as a compression driver of magnetized plasma targets to fusion conditions.

#### A. Experimental and Diagnostic Setups

Fig. 4 shows the six-gun configuration, i.e., a hexagonal arrangement with  $24^\circ$  between adjacent guns. We can fire all six guns simultaneously or any arbitrary subset of them. We often fired two or three guns for better diagnostic access to and interpretation of plasma-shock evolution between adjacent merging jets.

Table II summarizes the specifications of the capacitor banks driving the six plasma guns. Each gun has an integrated capacitor bank ( $-5 \text{ kV}$ ,  $575 \mu\text{F}$ , and  $7.2 \text{ kJ}$ ) driving the main electrode discharge. A separate capacitor bank ( $12 \text{ kV}$ ,  $96 \mu\text{F}$ , and  $6.9 \text{ kJ}$ ) drives all six GVs of the six guns, and yet another separate capacitor bank ( $30 \text{ kV}$ ,  $12 \mu\text{F}$ , and  $5.4 \text{ kJ}$ ) drives all six PI systems. A final capacitor bank



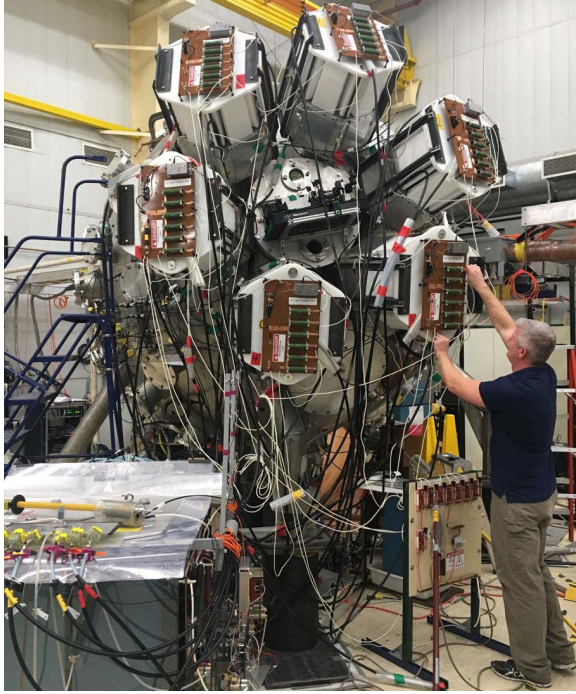


Fig. 4. Photograph (taken on January 31, 2017) of the PLX facility at LANL with six PLX- $\alpha$  coaxial guns mounted in a hexagonal pattern on a 2.74-m spherical vacuum chamber. The large port in the middle of the hexagon provides the launch positions of seven chords of a fiber-coupled, visible interferometer [see also Fig. 6(a)]. The cart at the lower left holds the capacitor banks that power the GV and PI systems for all six guns.

TABLE II  
CAPACITOR-BANK SPECIFICATIONS FOR THE  
SIX-GUN PLX- $\alpha$  EXPERIMENTS AT LANL

Banks	Capacitor (#/bank)	Total bank capacitance ( $\mu$ F)	Rated bank voltage (kV)
Gun electrodes	NWL 13339 (18)	575 per gun	-5
Gas valve (GV)	Maxwell 32567 (4)	96 for 6 guns	12
Pre-ionizers (PI)	Maxwell 32814 (2)	12 for 6 guns	30
Master trigger (MT)	Maxwell 32814 (1)	6 for 6 guns	-30

(-30 kV, 6  $\mu$ F, and 2.7 kJ) drives the master-trigger (MT) system for all six guns. Typical operation on the PLX has utilized -4.5, 8.5, 24, and -28 kV for the gun-electrode, GV, PI, and MT banks, respectively.

All banks are switched by high-voltage, high-current spark-gap switches custom made by HyperV Technologies. Each 575- $\mu$ F bank driving the gun electrodes consists of six separate sub-banks driven by six separate spark-gap switches. These switches (six per gun, and 36 total for six guns) are triggered by the MT bank. The switches are pressurized to various static pressures with either Ar or Ar/N<sub>2</sub> (90%/10%) mixture (gun switches) or N<sub>2</sub> (GV, PI, and MT switches); the switch gasses are purged for 15–30 s after each experimental shot. All switches are triggered by optically coupled signals that largely eliminate noise-induced misfires. Fig. 5 shows sample

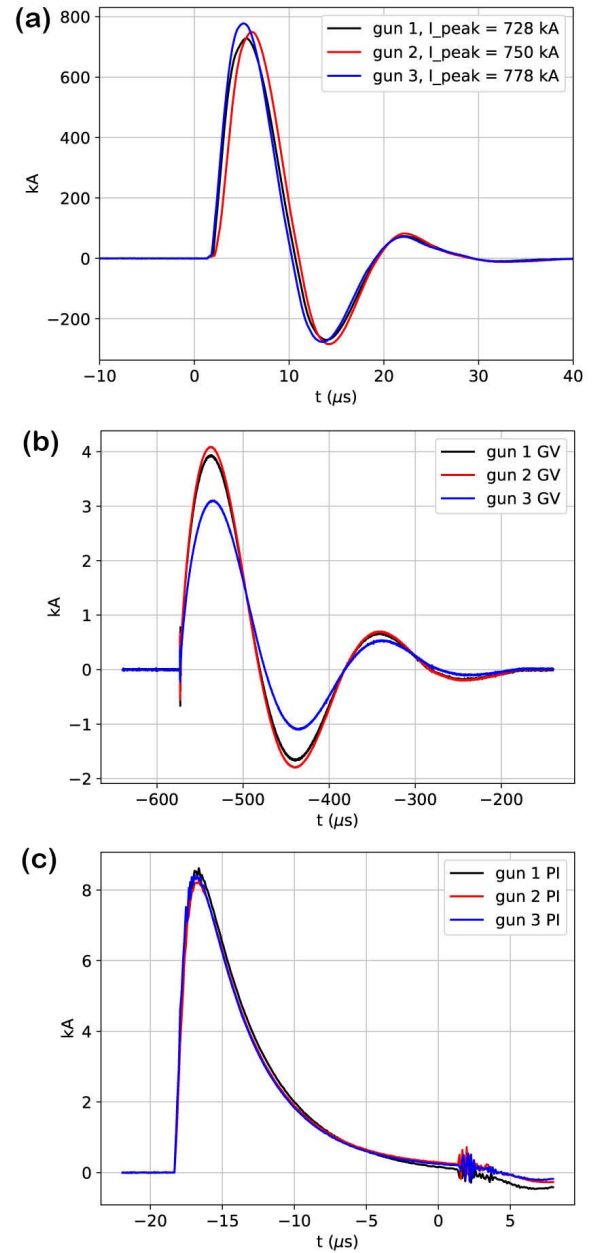


Fig. 5. Electrical-current waveforms, measured by Rogowski coils, for (a) gun electrodes, (b) GVs, and (c) PIs for a representative three-gun experiment (shot 1062; charge voltages: 5 kV for the gun electrodes, 10 kV for the GVs, and -24 kV for the PIs). These waveforms were absolutely calibrated to units of kiloamperes by equating the time-integrated value of each signal with the known, stored charge in their respective capacitor banks.

electrical currents from the gun, GV, and PI banks for a three-gun experiment. Note the large imbalance for one of the GV currents; this is consistent with observed jet-to-jet imbalance leading to ongoing improvements in the GV design and power delivery, as discussed in Section III-B4.

Diagnostics for the six-gun experiments are summarized in Table III. The 12-chord, fiber-coupled, visible interferometer (using a 320-mW, 651-nm solid-state laser and upgraded from a previous eight-chord system [35], [36]) and broadband visible survey spectrometer have both been described in detail elsewhere [7], [13]. The survey-spectrometer detector (0.160-nm/pixel resolution at 510 nm) is now upgraded to

TABLE III  
SUMMARY OF DIAGNOSTICS FOR THE SIX-JET EXPERIMENTS

Diagnostic	Measurement	Parameter(s) inferred
12-chord interferometer	phase shift (time resolved)	line-integrated electron density ( $n_e \ell$ )
survey spectrometer	visible line spectra (time gated)	chord-averaged $n_e$ , $T_e$ , $Z$
high-resolution spectrometer	visible line spectra (time gated)	line-integrated $T_i$ and Doppler shift
photodiode array	visible light (time resolved)	$V_{jet}$ and axial profile
CCD camera (single frame)	visible image (time gated)	$V_{jet}$ and global plasma appearance
CCD camera (12 frames)	visible image sequence (time gated)	same as above and plasma evolution

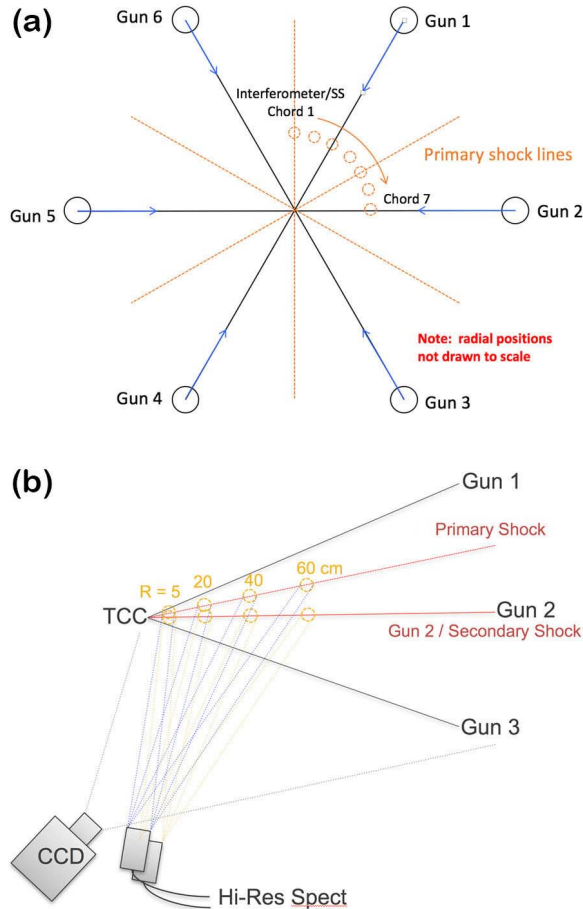


Fig. 6. (a) Projected view of interferometer chords 1–7 with respect to the location of the six guns as viewed from behind the guns. The chords go straight across the chamber maintaining parallel separation, whereas the guns point toward target chamber center (TCC). The survey-spectrometer collection optic is moved around to overlap with any of the seven interferometer chords. In the projected plane (as depicted), the arc formed by the interferometer chords is 5.7 cm from TCC. However, where chords 3 and 5 actually intersect the jet-propagation axes is 14.7 cm from TCC. (b) CCD-camera (single frame) and Doppler-spectroscopy viewing positions (side-on view of the jets propagating toward TCC). The two Doppler-spectroscopy chords can be separately moved around to the various radii shown along the “primary-shock” line or the “secondary-shock” line.

a PI-MAX2 intensified charge-coupled-device (CCD) camera ( $1024 \times 256$  pixels, 16-bit dynamic range, and typical exposure of 1–2  $\mu$ s), and the collection optic has also been upgraded

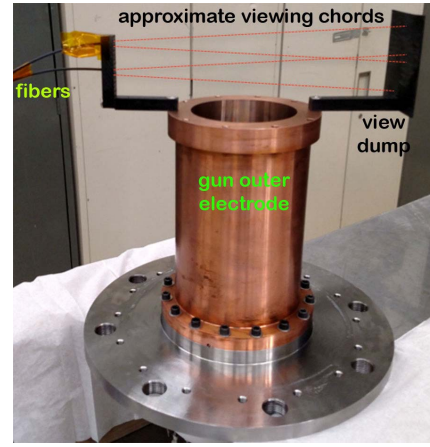


Fig. 7. Photograph showing the two photodiode views that provide precise measurements of the plasma-jet velocity just beyond the end of the gun nozzle. The photodiode mounting structures and view dump are made from Noryl, chosen for its electrical-insulation and low-outgassing properties.

such that the diameter of the viewing chord at the positions of interest within the plasma is about 1 cm. Their setups (initially, using only seven of the twelve interferometer chords) are shown in Fig. 6(a). The high-resolution spectrometer is a 4-m McPherson 2062DP, with  $2400 \text{ mm}^{-1}$  grating (1.52 pm/pixel at 480.6 nm), coupled to a Stanford Computer Optics 4 Quik E intensified-CCD camera ( $752 \times 482$  pixels, 10-bit dynamic range, and typical exposure of 1  $\mu$ s); plasma light is collected at a chamber window with two 2-in, 100-mm achromatic lenses [Fig. 6(b)] and transported to the spectrometer with a bifurcated  $80 \times 100 \mu\text{m}$ -core fiber bundle (so that two views can be recorded simultaneously). The diameter of the viewing chords at the positions of interest is about 1.5 cm. For the photodiode arrays, two channels of light are collected through 1-mm, 5/16-in-deep pinholes near the end of each gun nozzle (Fig. 7) and transported through optical fibers (SH-4001) to a photodiode-array board that digitizes the signals at 100 MHz with 14-bit dynamic range. The light level received at the photodiode board can be attenuated by physically adjusting the distance between a gap in each fiber. The single-frame intensified-CCD camera is a DiCam Pro ICCD ( $1280 \times 1024$  pixels with 12-bit dynamic range), positioned as shown in Fig. 6(b), and the 12-frame intensified-CCD camera is an Invisible Vision UHSi 12/24 ( $1000 \times 860$  pixels with 12-bit dynamic range).

### B. Initial Diagnostic Results

In this section, we present initial sample results from key diagnostics from a series of three- and six-gun experiments; all shots reported here used argon. These were our first full experimental campaigns, and thus jet performance was not yet optimized. Furthermore, we operated well below peak powers/energies of our capacitor banks, as we were exploring parameter space and did not wish to push the limits of our systems yet.

1) *CCD-Camera Images*: Fig. 8 shows time series of intensified-CCD camera images (from the single-frame DiCam Pro) from three- and six-gun experiments, showing the formation of “primary” shocks (due to merging of adjacent jets) and



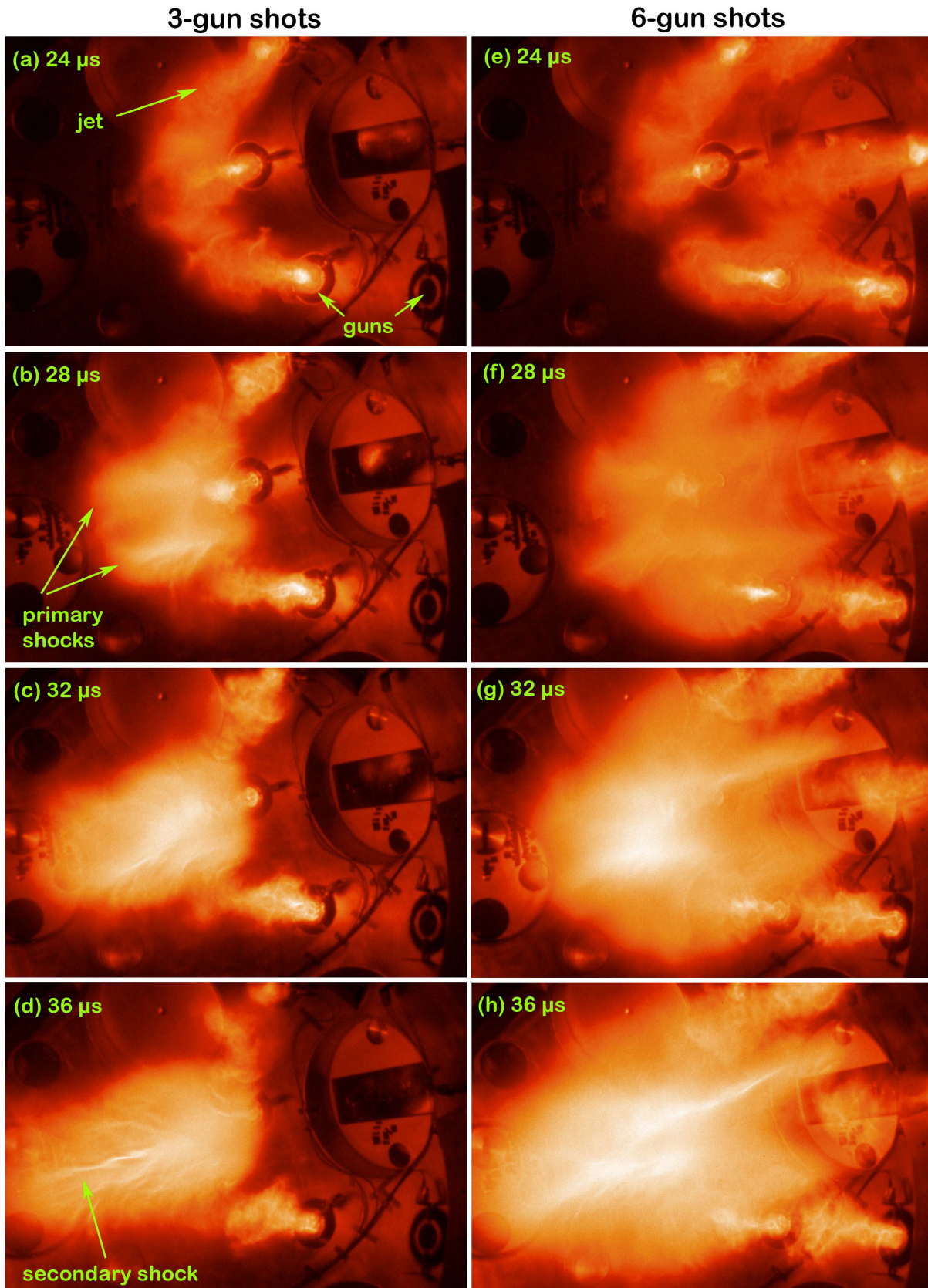


Fig. 8. Intensified-CCD camera images (10-ns exposure, logarithm of intensity, false color, and cropped to  $1280 \times 850$  pixels each) showing the evolution of (a)–(d) three-gun (shots 1064, 1066, 1061, and 1069) and (e)–(h) six-gun experiments (shots 1007, 1038, 1041, and 1043). As labeled in the three-gun image sequence, (b) primary shocks form along the merge plane of adjacent jets and (d) (presumed) secondary shocks form due to subsequent merging of the primary-shock plasmas.

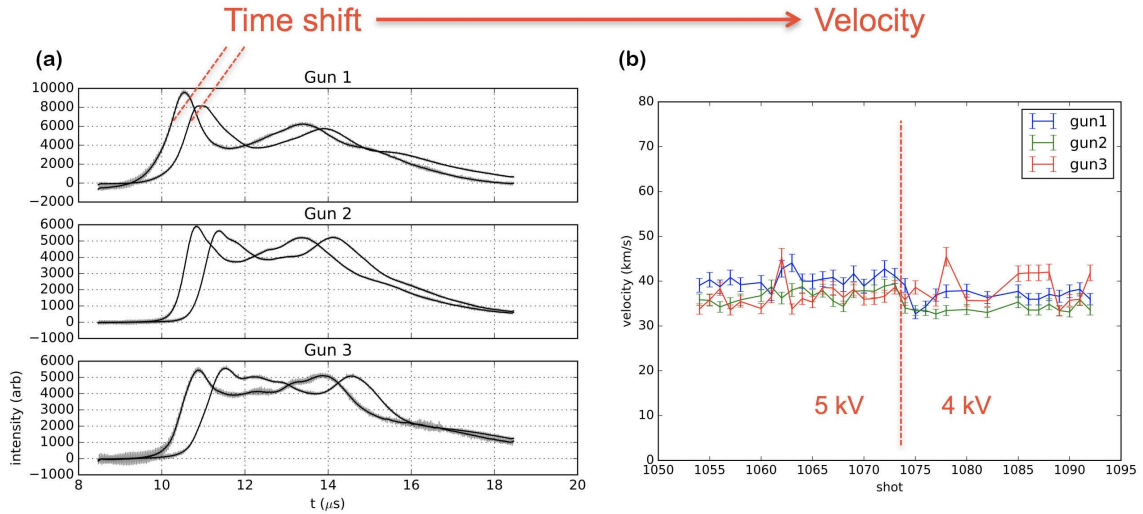


Fig. 9. (a) Sample photodiode signals versus time from three guns. For each gun, photodiode viewing chords are spaced 2 cm apart and oriented transverse to the direction of jet propagation (see Fig. 7). (b) Inferred  $V_{\text{jet}}$  for an ensemble of shots at two gun charge voltages (4 and 5 kV).

presumed “secondary” shocks (due to subsequent merging of the initial merged, shocked plasmas). Detailed prior diagnostic studies [14], [15] of plasma jets with similar densities and velocities showed, through quantitative diagnostic measurements and analyses, that what we are calling primary shocks is consistent with collisional oblique shocks forming along the merge plane of adjacent jets. Primary and secondary shocks were both also observed and studied in 3-D hydrodynamic simulations [25].

2) *Photodiode Arrays*: These provide measurements of  $V_{\text{jet}}$ . Light is collected as shown in Fig. 7; a view dump eliminates pickup of stray light and reflections. Fig. 9 shows sample photodiode and the inferred  $V_{\text{jet}}$  values. The latter are determined by dividing the distance (2 cm) by the time shift that maximizes the correlation between the two normalized photodiode signals from each gun. For the data set presented in Section III-B,  $V_{\text{jet}}$  is generally in the range 30–45 km/s.

3) *Doppler Spectroscopy*: This provides ion-temperature  $T_i$  measurements at the shock region between two merging plasma jets as shown in Fig. 6(b). Fig. 10(a) shows an example of the data from the CCD detector. Fig. 10(b) and (c) show the data, instrumental-broadening profile, and the best fit to the data of a Gaussian convolved with the instrumental profile, for the secondary-shock and primary-shock views, respectively. For the cases shown in Fig. 10,  $T_i = 6.0 \pm 0.13$  and  $4.3 \pm 0.11$  eV at  $t = 42 \mu\text{s}$  and  $R = 20$  cm along the secondary and primary shock lines, respectively. Based on this time and viewing position,  $T_i = 6.0$  eV is likely indicative of  $T_i$  of the secondary-shock plasma. We have also observed up to  $T_i \sim 30$  eV (for argon) at the time ( $t \approx 25 \mu\text{s}$ ) and spatial position ( $R \approx 50$ – $60$  cm) of the primary shock, but  $T_i$  cools quickly (over  $\sim 10 \mu\text{s}$ ) by equilibrating with electrons (full results on ion shock heating/dynamics for different gas species will be reported elsewhere). As discussed in the following in the survey-spectroscopy section,  $T_e$  remains much colder throughout the primary and secondary shock-formation process.

Measurement of ion heating as an essential property of collisional plasma shocks [37] is an interesting study in its own right, which we are pursuing as part of a separate project on the experimental study of plasma shocks. Here, our interest in shock ion heating is to provide constraining data in order to properly assess its role in degrading the jet/liner  $M \sim C_s^{-1} \sim (T_e + T_i)^{-1/2}$ . Because  $T_e$  does not increase much throughout the jet-merging process [15], [16] (also see survey-spectroscopy results in the following) due to strong thermal and radiative loss rates, ion heating dominates the  $M$  degradation. The latter would lead to stronger liner spreading and is predicted to seriously degrade the ability of the liner to compress a magnetized target plasma to reactor-relevant fusion conditions [34]. Ongoing research using two-temperature (2T) hydrodynamic simulations (see Section IV-A) is investigating the role of ion shock heating on plasma-liner formation, convergence, and performance.

4) *Multichord Interferometry*: Multichord interferometry is used to measure  $\langle n_e \ell \rangle$  and to assess its variation across the spatial arc of the interferometer chords shown in Fig. 6(a). Fig. 11(a) shows an example of  $\langle n_e \ell \rangle$  for each of the seven chords versus time. Fig. 11(b) shows a comparison between  $\langle n_e \ell \rangle$  ( $t = 36 \mu\text{s}$ , averaged over shots 1019–1032) and synthetic data from a 3-D hydrodynamic simulation of the six-gun experiment (see Section IV-A for a description of the simulation). From the synthetic data, it can be seen that chords 1 and 5 are predicted to have the highest values of  $\langle n_e \ell \rangle$ , consistent with those chords intersecting the position of primary shocks [see Fig. 6(a)]. Similarly, chords 3 and 7 are predicted to have the lowest values of  $\langle n_e \ell \rangle$ , consistent with those chords intersecting the position of jets.

Two key, initial conclusions are drawn from the comparison between experimental and synthetic interferometry data: 1) very good agreement of the order-of-magnitude of  $\langle n_e \ell \rangle$  gives us confidence in our knowledge of the jet parameters and leading-order accuracy of the simulations and 2) poor agreement in the variation of  $\langle n_e \ell \rangle$  versus chord number is



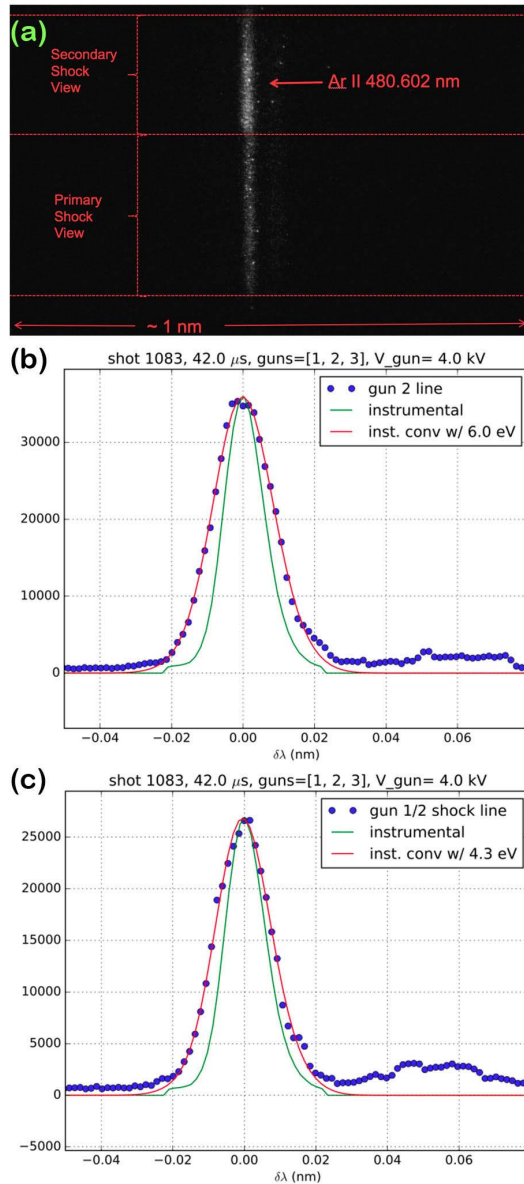


Fig. 10. (a) High-resolution-spectroscopy data (shot 1083, 1- $\mu\text{s}$  exposure) showing two views of a singly ionized argon spectral line, corresponding to the  $R = 20$ -cm positions shown in Fig. 6(b). The vertical and horizontal axes represent the height of the spectrometer slit and wavelength, respectively. (b) Vertically integrated signal (arb.) versus wavelength (centered at 480.602 nm) for the secondary-shock-line view ( $T_i = 6.0 \pm 0.13$  eV) and (c) primary-shock-line view ( $T_i = 4.3 \pm 0.11$  eV), from (a). The error quoted for  $T_i$  is the curve-fitting error assuming Poisson weighting of the spectral data.

indicative of insufficient balance (in mass and/or velocity) among jets, and thus the symmetry seen in the synthetic data (e.g., between chords 1/5, 3/7, and so on) is not reproduced in the experiment. The lack of symmetry over a wide range of time is also apparent in Fig. 11(a). Numerical simulations of six-jet experiments that incorporate unbalanced jet velocities and/or trigger times are aiding our interpretation of these data (see Section IV-A for further discussion). In order to improve the jet-to-jet balance, we plan to upgrade our GVs and have also added the ability to fine tune (through variable resistances and inductances) the electrical characteristic of

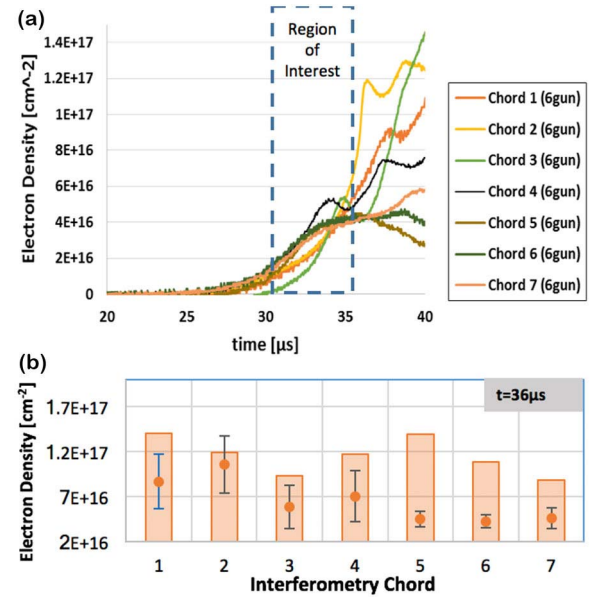


Fig. 11. (a) Line-integrated electron density  $\langle n_e \ell \rangle$  versus time (shot 1008) from multichord interferometry [based on the setup in Fig. 6(a)]. “Region of interest” refers to the approximate time duration when jets merge to form a liner section. (b) Data points are  $\langle n_e \ell \rangle$  ( $t = 36$   $\mu\text{s}$ , averaged over shots 1019–1032) versus the chord number; error bars are the standard deviation over the shot range. The bars are synthetic data from 3-D SPFMMax hydrodynamic simulations of the six-gun experiments (see Section IV-A).

each of the six GV transmission lines. The new GVs (rev. 10) will provide higher precision and repeatability in the amount of mass injected. Varying the resistance/inductance of the GV transmission lines has already allowed us to tune the jet injected mass and velocity, as observed in the rise in chamber pressure after each shot, photodiode signals, and camera images.

5) *Survey Spectroscopy*: By comparing survey-spectroscopy data with non-local-thermodynamic-equilibrium (non-LTE) PrismSPECT [38] spectral calculations that utilize  $n_e$  values consistent with interferometry data, we are able to place bounds on  $T_e$  and  $\bar{Z}$  of the observed plasma volume; this methodology was previously described in detail [13] and applied in multiple experimental configurations [13]–[16], [39]. Fig. 12(a) shows an example of spectra from several viewing chords, showing that there is little variation over these chords. The chords intersect the jet-propagation axes at approximately 14.7 cm. Fig. 12(b) shows an example of a comparison between data and spectral calculations, showing good agreement for a calculation that assumes  $n_e = 10^{15}$  cm $^{-3}$  and  $T_e = 1.6$  eV (for which  $\bar{Z} = 0.99$ ). On the other hand, for calculations assuming  $T_e \leq 1.5$  eV or  $T_e \geq 1.9$  eV, the agreement between the spectral data and PrismSPECT calculations becomes dramatically worse, implying that  $1.5 < T_e < 1.9$  over a large spatial area and temporal range for the merging plasma jets.

#### IV. NUMERICAL MODELING

In this section, we provide a brief overview of the modeling research in support of the PLX- $\alpha$  project. However, detailed modeling results will be reported elsewhere.



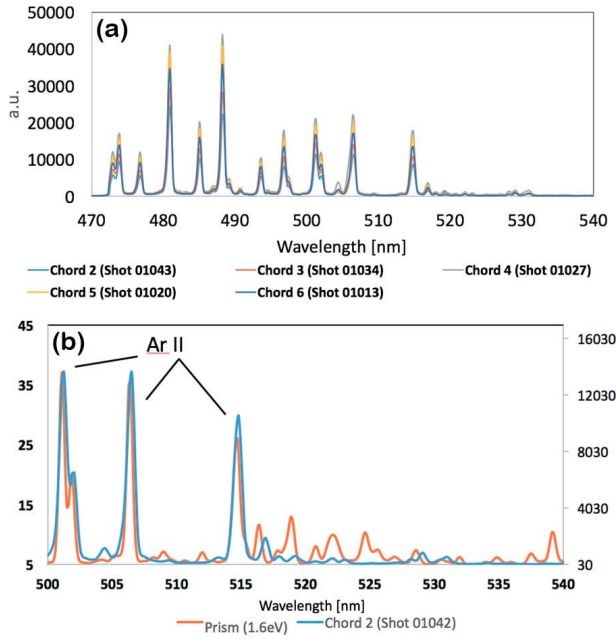


Fig. 12. (a) Visible survey spectra ( $t = 38 \mu\text{s}$ ,  $2\text{-}\mu\text{s}$  exposure) versus wavelength for views corresponding to interferometer chords 2–6 [see Fig. 6(a)] for six-gun argon experiments. (b) Comparison of survey-spectrometer data ( $t = 32 \mu\text{s}$  and  $2\text{-}\mu\text{s}$  exposure) and a PrismSPECT spectral calculation assuming  $n_e = 10^{15} \text{ cm}^{-3}$  and  $T_e = 1.6 \text{ eV}$ .

### A. Plasma-Liner Formation and Convergence

We use two 3-D hydrodynamic codes to simulate jet merging (two, three, and six guns) and spherical ( $4\pi$ ) plasma-liner formation and convergence (18–600 guns). The former are in support of our ongoing experiments (studying shock dynamics between merging jets and/or forming a section of a liner with six jets). The latter are to guide our preparation for planned  $4\pi$  experiments over the next two years.

The two 3-D codes being used are SPFMax [40], a smoothed-particle-hydrodynamic code, and FronTier [41], a hydrodynamic code with front tracking. As part of the PLX- $\alpha$  project, we have performed significant benchmarking of the codes against jet-merging experimental results, and we have added physics capabilities to the codes, including Braginskii thermal transport and viscosity [42], optically thin radiation loss, advanced EOS table lookup (using custom-generated non-LTE PROPACEOS tables [43] from Prism Computational Sciences), and  $2T$  (i.e., separate  $T_i$  and  $T_e$  evolution) modeling.

SPFMax and FronTier have been used to simulate three- and six-jet merging to guide diagnostics setup, generate synthetic data [see Fig. 11(b)] for comparisons with the diagnostic data, and aid our understanding of the comparisons. For generating the synthetic data in Fig. 11(b), we ran SPFMax using the six-gun setup of Fig. 6(a) with the following initial argon-jet parameters: velocity of  $35.8 \text{ km/s}$ ,  $T_i = T_e = 2.5 \text{ eV}$ , ion density  $n_i = 3.17 \times 10^{16} \text{ cm}^{-3}$ , diameter of  $8.5 \text{ cm}$ , length of  $10 \text{ cm}$ , and leading edge of the jets at  $R = 130 \text{ cm}$ . The simulation included non-LTE argon EOS, single-group opacity,  $2T$ , and ion and electron thermal conduction. To help understand the disagreement between the experimental and synthetic interferometry seen in Fig. 11(b), we

ran six-jet FronTier simulations that included random variations among jet velocities (up to 10%) and/or trigger times (up to  $1 \mu\text{s}$ ); these results show that the symmetry of primary- and secondary-shock formation is indeed drastically degraded compared with the case with identical jet velocities/timings (further motivating our ongoing efforts to improve the jet-to-jet balance). We also plan to use VISRAD [44] to generate synthetic spectral data to compare with spectroscopy data.

The  $4\pi$  simulations (with up to  $N = 600$  jets) have focused on studies of liner uniformity and ram-pressure ( $\rho v^2$ ) evolution as the liner forms and converges radially toward stagnation. For  $N \leq 60$ , the simulations directly inform planned PLX- $\alpha$  experiments, which aim to form  $4\pi$  imploding liners with 36–60 jets and  $\sim 100\text{--}150 \text{ kJ}$  of total liner kinetic energy, and predict peak  $\rho v^2 \sim 50 \text{ kbar}$ . For  $N > 60$ , the simulations are assessing the jet and uniformity requirements to achieve fusion-relevant conditions, requiring total liner kinetic energy of  $\gtrsim 30 \text{ MJ}$  and peak  $\rho v^2 \gtrsim 150 \text{ Mbar}$  [3], [34].

### B. Plasma-Liner Compression of a Magnetized Target

A separate modeling task is studying plasma-liner compression of a magnetized target in 1-D and 2-D, using the multifluid magnetohydrodynamic code USim [45]. A major purpose of this task is to identify and optimize PJMIF configurations with energy gain, guided by the results of [3] and [34]. New physics capabilities have also been added to USim as part of the PLX- $\alpha$  project, including optically thin radiation loss, non-LTE tabular EOS table lookup (also using PROPACEOS tables [43]), Braginskii viscosity [42], and  $\alpha$ -particle energy deposition based on the model implemented in [34]. A second important purpose of this task is to assess and understand the degradation of energy gain in going from 1-D to 2-D and to examine the further degradation of energy gain when nonuniformities (based on the work described in Section IV-A) are imposed on the liner/target interface, which exacerbate the Rayleigh–Taylor instabilities at the stagnating interface. Indeed, one specific objective of this task is to set requirements on the liner uniformity for PJMIF to remain viable as a fusion-energy concept.

## V. CONCLUSION AND PLANS

We have described an experiment to form and characterize a section of a spherically imploding plasma liner, as a development step toward PJMIF [1], [2]. This work is the first phase of the ARPA-E-sponsored PLX- $\alpha$  project, which aims to culminate with the formation and study of a spherically imploding plasma liner (as a standoff MIF compression driver) formed by merging 36–60 supersonic plasma jets. The latter are launched by newly developed coaxial plasma guns fabricated by HyperV Technologies Corp. (now owned by new fusion startup HyperJet Fusion Corporation).

This paper reports key early results from the PLX- $\alpha$  project: 1) design and operation of the new HyperV coaxial plasma guns and characterization of plasma-jet parameters; 2) completion of the PLX facility/diagnostic upgrades for six-gun experiments; 3) successful operation of up to six plasma guns and key diagnostics (photodiode arrays, fast imaging cameras,

survey spectroscopy, high-resolution spectroscopy, and multi-chord interferometry); and 4) diagnostic results showing that the key potentially deleterious physics issues associated with jet merging (e.g., ion shock heating leading to Mach-number-degradation and the seeding of nonuniformities that may exacerbate deceleration-phase instabilities of the liner/target interface in future target-compression experiments) can now be studied in a serious manner; these studies are ongoing and further details and conclusions will be reported elsewhere.

Ongoing three- and six-jet experiments are providing comprehensive data sets on ion shock heating for several plasma-jet species (H, He, N, Ne, Ar, Kr, and Xe) and two different jet-merging angles. Upon installation of improved GVs, which are expected to improve the jet-to-jet balance, we will then focus on obtaining more interferometry data to better assess the uniformity of the liner section formed by merging six jets [i.e., the setup shown in Fig. 6(a)]. Finally, we are incorporating a number of engineering improvements to the coaxial plasma guns to maximize both the assembly/operational efficiency and quality/quantity of experimental data for planned experiments with 36–60 guns to form  $4\pi$  spherically imploding plasma liners (over the next two years). These experiments will provide critical data on the magnitude and evolution of liner nonuniformity and ram pressure during radial convergence, to allow continued technical assessment and development of the PJMIF concept.

#### ACKNOWLEDGMENT

The authors thank R. Aragonez, R. Martinez (dec.), J. Vaughan, and M. Luna for valuable technical contributions, and Dr. G. Wurden for loaning numerous items of diagnostic hardware. They would also like to acknowledge the DOE Office of Fusion Energy Sciences for sponsoring PLX construction and research (2009–2012) and plasma-gun development by HyperV Technologies Corp. (2005–2012). Section III summarizes the invited talk by S. Hsu and posters by S. Langendorf and K. Yates that were presented at the International Conference on Plasma Science, Atlantic City, NJ, USA, May 22–25, 2017.

#### REFERENCES

- [1] Y. C. F. Thio *et al.*, "Magnetized target fusion in a spheroidal geometry with standoff drivers," in *Proc. 2nd Int. Symp. Current Trends Int. Fusion Res.*, 1999, p. 113.
- [2] S. C. Hsu *et al.*, "Spherically imploding plasma liners as a standoff driver for magnetoinertial fusion," *IEEE Trans. Plasma Sci.*, vol. 40, no. 5, pp. 1287–1298, May 2012.
- [3] C. E. Knapp and R. C. Kirkpatrick, "Possible energy gain for a plasma-liner-driven magneto-inertial fusion concept," *Phys. Plasmas*, vol. 21, no. 17, p. 070701, 2014.
- [4] I. R. Lindemuth and R. C. Kirkpatrick, "Parameter space for magnetized fuel targets in inertial confinement fusion," *Nucl. Fusion*, vol. 23, no. 3, p. 263, 1983.
- [5] R. C. Kirkpatrick, I. R. Lindemuth, and M. S. Ward, "Magnetized target fusion: An overview," *Fusion Technol.*, vol. 27, no. 3, pp. 201–214, 1995.
- [6] I. R. Lindemuth and R. E. Siemon, "The fundamental parameter space of controlled thermonuclear fusion," *Amer. J. Phys.*, vol. 77, no. 5, pp. 407–416, 2009.
- [7] S. C. Hsu *et al.*, "Laboratory plasma physics experiments using merging supersonic plasma jets," *J. Plasma Phys.*, vol. 81, no. 2, p. 345810201, 2015.
- [8] S. C. Hsu, "Technical summary of the first U.S. plasma jet workshop," *J. Fusion Energy*, vol. 28, no. 3, pp. 246–257, 2009.
- [9] F. Witherspoon *et al.*, "Development of mini Railguns for the plasma liner experiment (PLX)," *Bull. Amer. Phys. Soc.*, vol. 56, no. 16, p. 311, 2011.
- [10] S. Brockington, A. Case, S. Messer, L. Wu, and F. D. Witherspoon, "The HyperV 8000 $\mu$ g, 50 km/s plasma Railgun for PLX," *Bull. Amer. Phys. Soc.*, vol. 57, no. 12, p. 134, 2012.
- [11] A. Case, S. Messer, S. Brockington, L. Wu, F. D. Witherspoon, and R. Elton, "Merging of high speed argon plasma jets," *Phys. Plasmas*, vol. 20, no. 1, p. 012704, 2013.
- [12] S. Messer, A. Case, L. Wu, S. Brockington, and F. D. Witherspoon, "Nonlinear compressions in merging plasma jets," *Phys. Plasmas*, vol. 20, no. 3, p. 032306, 2013.
- [13] S. C. Hsu *et al.*, "Experimental characterization of railgun-driven supersonic plasma jets motivated by high energy density physics applications," *Phys. Plasmas*, vol. 19, no. 12, p. 123514, 2012.
- [14] E. C. Merritt, A. L. Moser, S. C. Hsu, J. Loverich, and M. Gilmore, "Experimental characterization of the stagnation layer between two obliquely merging supersonic plasma jets," *Phys. Rev. Lett.*, vol. 111, no. 8, p. 085003, 2013.
- [15] E. C. Merritt *et al.*, "Experimental evidence for collisional shock formation via two obliquely merging supersonic plasma jets," *Phys. Plasmas*, vol. 21, no. 5, p. 055703, 2014.
- [16] A. L. Moser and S. C. Hsu, "Experimental characterization of a transition from collisionless to collisional interaction between head-on-merging supersonic plasma jets," *Phys. Plasmas*, vol. 22, no. 5, p. 055707, 2015.
- [17] J. Loverich and A. Hakim, "Two-dimensional modeling of ideal merging plasma jets," *J. Fusion Energy*, vol. 29, no. 6, pp. 532–539, 2010.
- [18] J. T. Cassibry, R. J. Cortez, S. C. Hsu, and F. D. Witherspoon, "Estimates of confinement time and energy gain for plasma liner driven magnetoinertial fusion using an analytic self-similar converging shock model," *Phys. Plasmas*, vol. 16, no. 11, p. 112707, 2009.
- [19] R. Samulyak, P. Parks, and L. Wu, "Spherically symmetric simulation of plasma liner driven magnetoinertial fusion," *Phys. Plasmas*, vol. 17, no. 9, p. 092702, 2010.
- [20] T. J. Awe, C. S. Adams, J. S. Davis, D. S. Hanna, S. C. Hsu, and J. T. Cassibry, "One-dimensional radiation-hydrodynamic scaling studies of imploding spherical plasma liners," *Phys. Plasmas*, vol. 18, no. 7, p. 072705, 2011.
- [21] J. S. Davis, S. C. Hsu, I. E. Golovkin, J. J. MacFarlane, and J. T. Cassibry, "One-dimensional radiation-hydrodynamic simulations of imploding spherical plasma liners with detailed equation-of-state modeling," *Phys. Plasmas*, vol. 19, no. 10, p. 102701, 2012.
- [22] H. Kim, R. Samulyak, L. Zhang, and P. Parks, "Influence of atomic processes on the implosion of plasma liners," *Phys. Plasmas*, vol. 19, no. 8, p. 082711, 2012.
- [23] J. T. Cassibry, M. Stanic, S. C. Hsu, F. D. Witherspoon, and S. I. Abarzhi, "Tendency of spherically imploding plasma liners formed by merging plasma jets to evolve toward spherical symmetry," *Phys. Plasmas*, vol. 19, no. 5, p. 052702, 2012.
- [24] J. T. Cassibry, M. Stanic, and S. C. Hsu, "Ideal hydrodynamic scaling relations for a stagnated imploding spherical plasma liner formed by an array of merging plasma jets," *Phys. Plasmas*, vol. 20, no. 3, p. 032706, 2013.
- [25] H. Kim, L. Zhang, R. Samulyak, and P. Parks, "On the structure of plasma liners for plasma jet induced magnetoinertial fusion," *Phys. Plasmas*, vol. 20, no. 2, p. 022704, 2013.
- [26] D. D. Ryutov, "Adiabatic compression of a dense plasma 'mixed' with random magnetic fields," *Fusion Sci. Technol.*, vol. 56, no. 4, pp. 1489–1494, 2009.
- [27] D. R. Welch, T. C. Genoni, C. Thoma, N. Bruner, D. V. Rose, and S. C. Hsu, "Simulations of magnetic field generation in unmagnetized plasmas via beat-wave current drive," *Phys. Rev. Lett.*, vol. 109, no. 22, p. 225002, 2012.
- [28] D. R. Welch, T. C. Genoni, C. Thoma, D. V. Rose, and S. C. Hsu, "Particle-in-cell simulations of laser beat-wave magnetization of dense plasmas," *Phys. Plasmas*, vol. 21, no. 3, p. 032704, 2014.
- [29] Y. C. F. Thio, J. T. Cassibry, and T. E. Markusic, "A concept for directly coupled pulsed electromagnetic acceleration of plasmas," in *Proc. 38th AIAA/ASME/SAE/ASEE Joint Propuls. Conf. Exhib.*, 2002, pp. 1–9. [Online]. Available: <http://ntrs.nasa.gov/archive/nasa/casi.ntrs.nasa.gov/20030002753.pdf>
- [30] J. T. Cassibry, Y. C. F. Thio, and S. T. Wu, "Two-dimensional axisymmetric magnetohydrodynamic analysis of blow-by in a coaxial plasma accelerator," *Phys. Plasmas*, vol. 13, no. 5, p. 053101, 2006.

- [31] F. D. Witherspoon *et al.*, "A contoured gap coaxial plasma gun with injected plasma armature," *Rev. Sci. Instrum.*, vol. 80, no. 8, p. 083506, 2009.
- [32] R. E. Peterkin, M. H. Frese, and C. R. Sovinec, "Transport of magnetic flux in an arbitrary coordinate ALE code," *J. Comput. Phys.*, vol. 140, no. 1, pp. 148–171, 1998.
- [33] A. Case, S. Messer, R. Bomgardner, and F. D. Witherspoon, "Interferometer density measurements of a high-velocity plasmoid," *Phys. Plasmas*, vol. 17, no. 5, p. 053503, 2010.
- [34] S. J. Langendorf and S. C. Hsu, "Semi-analytic model of plasma-jet-driven magneto-inertial fusion," *Phys. Plasmas*, vol. 24, no. 3, p. 032704, 2017.
- [35] E. C. Merritt, A. G. Lynn, M. A. Gilmore, and S. C. Hsu, "Multi-chord fiber-coupled interferometer with a long coherence length laser," *Rev. Sci. Instrum.*, vol. 83, no. 3, p. 033506, 2012.
- [36] E. C. Merritt, A. G. Lynn, M. A. Gilmore, C. Thoma, J. Loverich, and S. C. Hsu, "Multi-chord fiber-coupled interferometry of supersonic plasma jets (invited)," *Rev. Sci. Instrum.*, vol. 83, no. 10, p. 10D523, 2012.
- [37] M. Y. Jaffrin and R. F. Probstein, "Structure of a plasma shock wave," *Phys. Fluids*, vol. 7, no. 10, pp. 1658–1674, 1964.
- [38] J. J. MacFarlane *et al.*, "Simulation of the ionization dynamics of aluminum irradiated by intense short-pulse lasers," in *Proc. Inertial Fusion Sci. Appl.*, 2004, p. 457.
- [39] C. S. Adams, A. L. Moser, and S. C. Hsu, "Observation of Rayleigh-Taylor-instability evolution in a plasma with magnetic and viscous effects," *Phys. Rev. E*, vol. 92, no. 5, p. 051101(R), 2015.
- [40] J. T. Cassibry, R. Cortez, C. Cody, S. Thompson, and L. Jackson, "Three dimensional modeling of pulsed fusion for propulsion and terrestrial power using smooth particle fluid with Maxwell equation solver (SPFMax)," in *Proc. 53rd AIAA/SAE/ASEE Joint Propuls. Conf. AIAA Propuls. Energy Forum*, 2017, p. 4677. [Online]. Available: <https://doi.org/10.2514/6.2017-4677>.
- [41] R. Samulyak, J. Du, J. Glimm, and Z. Xu, "A numerical algorithm for MHD of free surface flows at low magnetic Reynolds numbers," *J. Comput. Phys.*, vol. 226, no. 2, pp. 1532–1549, 2007.
- [42] S. I. Braginskii, "Transport processes in a plasma," in *Reviews of Plasma Physics*, vol. 1, M. A. Leontovich, Ed. New York, NY, USA: Consultants Bureau, 1965, p. 205.
- [43] J. J. MacFarlane, I. E. Golovkin, and P. R. Woodruff, "HELIOS-CR—A 1-D radiation-magnetohydrodynamics code with inline atomic kinetics modeling," *J. Quant. Spectrosc. Radiat. Transf.*, vol. 99, pp. 381–397, May/Jun. 2006.
- [44] J. J. MacFarlane, "VISRAD—A 3-D view factor code and design tool for high-energy density physics experiments," *J. Quant. Spectrosc. Radiat. Transf.*, vol. 81, nos. 1–4, pp. 287–300, 2003.
- [45] K. Beckwith, S. Veitzer, S. McCormick, J. Ruge, L. N. Olson, and J. C. Cahoun, "Fully implicit ultrascale physics solvers and application to ion source modeling," *IEEE Trans. Plasma Sci.*, vol. 43, no. 4, pp. 957–964, Apr. 2015.

Authors' photographs and biographies not available at the time of publication.